PAPER

Shock temperature and reflectivity of precompressed H_2O up to 350 GPa: Approaching the interior of planets

Shock temperature and reflectivity of precompressed H_2O up to 350 GPa: Approaching the interior of planets*

Zhi-Yu He(贺芝宇)[1], Hua Shu(舒桦)[1], Xiu-Guang Huang(黄秀光)[1,2], Qi-Li Zhang(张其黎)[3], Guo Jia(贾果)[1], Fan Zhang(张帆)[1,†], Yu-Chun Tu(涂昱淳)[1], Jun-Yue Wang(王寓越)[4], Jun-Jian Ye(叶君建)[1], Zhi-Yong Xie(谢志勇)[1], Zhi-Heng Fang(方智恒)[1], Wen-Bing Pei(裴文兵)[1,2], and Si-Zu Fu(傅思祖)[1,2]

[1] *Shanghai Institute of Laser Plasma, CAEP, P. O. Box* 800-229, *Shanghai* 201800, *China*
[2] *IFSA Collaborative Innovation Center, Shanghai Jiaotong University, Shanghai* 200240, *China*
[3] *Institute of Applied Physics and Computational Mathematics, Beijing* 100088, *China*
[4] *Center for High Pressure Science and Technology Advance Research, Beijing* 100094, *China*

(Received 23 July 2018; revised manuscript received 20 September 2018; published online 10 November 2018)

Using a combination of static precompression and laser-driven shock compression, shock temperature and reflectivity of H_2O have been measured up to 350 GPa and 2.1×10^4 K. Here, two calibration standards were applied to enhance temperature measurement reliability. Additionally, in temperature calculations, the discrepancy in reflectivity between active probe beam wavelength and self-emission wavelength has been taken into account to improve the data's precision. Precompressed water's temperature–pressure data are in very good agreement with our quantum molecular dynamics model, suggesting a superionic conductor of H_2O in the icy planets' deep interior. A sluggish slope gradually approaching Dulong–Petit limit at high temperature was found at a specific heat capacity. Also, high reflectivity and conductivity were observed at the same state. By analyzing the temperature–pressure diagram, reflectivity, conductivity and specific heat comprehensively at conditions simulating the interior of planets in this work, we found that as the pressure rises, a change in ionization appears; it is supposedly attributed to energetics of bond-breaking in the H_2O as it transforms from a bonded molecular fluid to an ionic state. Such molecular dissociation in H_2O is associated with the conducting transition because the dissociated hydrogen atoms contribute to electrical properties.

Keywords: high temperature measurement, equation of state of water, laser-driven shock, diamond anvil cell

PACS: 62.50.–p, 51.30.+i, 64.30.–t, 52.25.Kn **DOI:** 10.1088/1674-1056/27/12/126202

1. Introduction

Water is ubiquitous in the universe. In the outer solar system, many satellites roughly the same size as or larger than moons such as Europa or Titan II are almost covered by water or ice.[1,2] Deep in the universe outside the solar system, characteristic spectral lines emitted by water molecules were observed in nebulae formed by large numbers of stars such as the Orion nebulae M42.[3] As a current hotspot, typical "ice giants" such as Neptune and Uranus are believed to contain significant amounts of water.[4] Materials on these planets are under high pressure by virtue of their own gravitational attraction.

Thus, the equation of state (EOS) of water in extreme conditions is important in understanding the composition and evolution of planets and their satellites as well as their distributions of density, pressure, and temperature. So far, ANEOS[5] and Sesame[6] models for water have been employed to model ice giants. However, quantum molecular dynamics (QMD) calculations and density-functional-theory-based molecular dynamics (DFT-MD) simulations of water[7–9] propose an EOS differing from ANEOS and Sesame. In fact, they were in good agreement with reported shock experiments.[10–12] MD models, which suggest a superionic H_2O with hydrogen ions moving within a solid lattice of oxygen in the deep interior of icy planets — for instance, Uranus and Neptune — at high densities and low temperature, propose dynamo models to explain magnetic field structure and predict that the ice giants contain no ice but dissociated water at high ionic conductivity.[10] However, studies on melting temperature of H_2O suggest that water remains in the liquid state even in deep interior conditions rather than in an ionic solid system.[13] These discrepancies from experiments and theoretical models have great impact on explaining planetary magnetic field formation.[14,15]

In fact, comparisons between shock experiments and theoretical EOS models on planetary interior structure rarely involve temperature, which has historically proven difficult to obtain. However, temperature is fundamental to thermodynamics and an important constraint to EOS models. Disagreement in various models' temperatures might lead to completely different results. Experimental measurement of water's

*Project supported by the National Key Research and Development Program of China (Grant No. 2017YFA0403200) and the Science Challenge Project (Grant No. TZ2016001).

†Corresponding author. E-mail: innocentman001@163.com

shock temperature is much more challenging than dynamic parameters such as pressure because directly measuring it is difficult and requires absolute measurement of self-emission intensity. Kanani K *et al.* attempted to measure the shock temperature of precompressed water, but came into great uncertainty of about 35% at pressure up to 250 GPa.[16] Melting temperature measurements of pressure below 100 GPa have been much reported.[13,17,18] Recently Kimura *et al.* measured precompressed water's P–ρ–T data up to 260 GPa.[11] Millot *et al.* measured temperature below 1000 K at pressure up to 300 GPa.[12] To validate EOS models, much more data and much higher temperature measurements at extremely high pressure are necessary.

Coupling static and dynamic compressions, shock experiments on precompressed samples can access states unreachable by either method alone, covering a broad range of P–ρ–T space and approaching conditions close to the isentrope of planets.[16,19,20]

Here, we present shock temperature and optical measurements on precompressed water via laser-driven shock waves that can generate high pressure and temperature conditions comparable with ice giant planets' interior conditions. Achieved temperatures lie between the principal Hugoniot and the principal isentrope of water via the precompression cell, thereby increasing access to icy giant planets' interior states. Additionally, specific heat and electrical conductivity inferred from Hugoniot data and reflectivity were analyzed for understanding icy giants' magnetic fields and layers.

2. Methods

2.1. Experimental procedure

Experiments were conducted at the "Shenguang-II" laser facility of the National Laboratory on High Power Laser and Physics. Decaying shock waves were generated by ablation of the thin plastic layer backing the sample. Energies of up to $\sim$ 1500 J were delivered at 351 nm using "the ninth laser beam". The laser's temporal profile is nearly square, with a rise and fall time of $\sim$ 300 ps and a full width at half maximum of $\sim$ 2 ns. The laser beam was smoothed using a lens-array (LA) system[21–23] to eliminate large-scale spatial modulation and to obtain a flat-topped profile in the focal plane. Characteristics of the optical system (lens + LA) were such that the focal spot had a 1 mm$\times$ 0.7 mm or 0.65mm $\times$0.65 mm rectangular region. Resulting intensities were from 0.5×10^{14} W/cm^2 to 2×10^{14} W/cm^2.

Standard laser-shock diagnostics were employed, including streaked optical pyrometry (SOP) and a line-imaging velocity interferometer system for any reflector (VISAR). SOP is used for observation of self-emission of the target from which temperature can be extracted, whereas VISAR (660 nm) is applied for simultaneous diagnostics on free surface velocity and optical reflectivity.[24–27] A schematic illustrating these diagnostics is shown in Fig. 1(b). The imaging system's first part (L1), composed of four achromatic lenses, produces a magnified real image. This real image is transmitted and collimated by combined lenses (L2-1 and L2-2). Then, it is imaged by L4 at the SOP streak camera's slit and recollimated by L3-1 and imaged by L3-2 at the VISAR streak camera's slit. The single-channel filter is a narrowband filter at (442 ± 20) nm that allows only blue light to pass. The specially designed beam splitter $M_{\mathrm{LR-WT}}$ is a dichroic mirror that reflects the probe beam (660 nm) to VISAR while transmitting the thermal emission to SOP. Diagnostic systems had a temporal resolution of $\sim$ 50 ps and a spatial resolution of $\sim$ 7 μm.

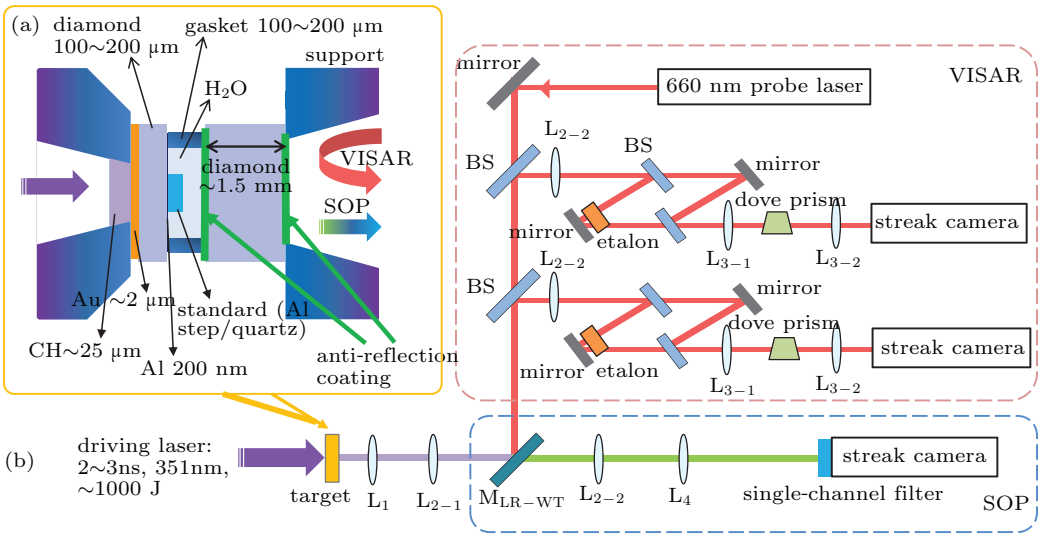

Fig. 1. (color online) (a) Schematic illustration of the DAC target; (b) Diagnostics design used to characterize the shocked sample. VISAR measures shock velocity and optical reflectivity. SOP observes thermal emission from the sample.

The target sample is shown in Fig. 1(a). Ultra-pure water was loaded into a diamond anvil cell (DAC) for precompression from 0.49 GPa to 0.63 GPa. The sample chamber was approximately 300 μm∼ 800 μm in diameter and 50 μm∼ 100 μm thick. Tungsten carbide (WC) supports allowed ample drive laser entry. Copper was selected as a gasket because it is easily deformed. The diamond on the drive laser side should be thin in order to obtain high dynamic loading pressure. On the other hand, a thin diamond would limit the static pressure of DAC. Thus, the designated thickness of the thin diamond was approximately 100 μm∼ 200 μm, whereas the thick diamond window on the diagnostic side was approximately 1.5 mm. Quartz or aluminum step was used as standard material for impedance matching[28] and placed against the diamond from which the shock wave enters. The thin diamond's drive laser side was coated with a polypropylene ablator of ∼ 25 μm and a gold x-ray preheat shield of ∼ 2 μm. An aluminum coating of ∼ 200 nm was on the standard material's drive laser side to increase reflectivity of the breakout from the thin diamond. Antireflection filters were coated on both sides of the thick diamond window to clarify the VISAR image. Initial pressure (P_0) was measured using the ruby fluorescence method[29] with an uncertainty of ∼ 0.03 GPa. The initial density and refractive index can be derived from the water EOS model at ambient pressure.[30] A detailed description of the target design in DAC can be seen elsewhere.[20,31]

2.2. Temperature measurement

Brightness temperature was achieved by the SOP system with a visible streak camera coupled to a narrow band (442 ± 20 nm) filter. Determination of temperature is possible because all bodies of finite temperature emit with a spectral radiance characteristic of their thermal state.[32] For shock temperature experiments that can be regarded as gray body, we relate temperature to spectral radiance $L(\lambda)$ by Planck's law

$$L(\lambda) = \frac{\varepsilon(\lambda)}{\lambda^5} \frac{2hc^2}{\exp(hc/\lambda kT) - 1}, \tag{1}$$

where h is Planck's constant, c is the speed of light, k is Boltzmann constant, λ is the wavelength of the SOP channel, and T is the temperature of the body. Emissivity ε is given by Kirchhoff's law as $\varepsilon(\lambda) = 1 - t(\lambda) - R(\lambda)$.[33] Transmissivity $t(\lambda)$ is assumed to be zero because the shock wave front is optically thick.[34] R is the reflectivity of shock front that can be extracted from VISAR[35] and was determined by comparing shock reflectivity to that from the aluminum surface, which has a known value of 80%±5%.

In our experiments, unshocked sample in front of the wavefront is transparent so that bright light emitted from shocked sample can be recorded by streaked camera of SOP. The counts of streaked camera correspond to the spectral radiance $L(\lambda)$. Similarly, the counts of two streaked cameras in the VISAR system correspond to the reflectivity's intensity. The influence of other possible luminous mechanisms on the intensity of $L(\lambda)$ and R can be excluded by controlling cameras' settings to make them work in the linear range, considering the transmittance of precompressed sample and making the target chamber operate in ultrahigh vacuum (∼ 10^{-3} Pa) with no stray light. In our experiments, reflectivity was obtained from the mean value of two cameras in the VISAR system and difference in reflectivity between the VISAR probe beam wavelength and the SOP channel wavelength has been taken into account. Details are included in Section 3.

Table 1. Experimental conditions (initial pressure, initial density and initial refractive index) and final values (shock velocity, pressure, temperature and reflectivity) of shock precompressed water samples at interface of standard and water. The initial refractive index is given by an empirical formula, $n_0 = 1.332 + 0.322(\rho_0 - 1)$. Temperaure of shot no. 018 and 019 failed to be estimated because the self-emissions were not obtained. Uncertainties of final values are listed below each measured value in parentheses. A more detailed list of the experiments would be published elsewhere.[31]

Shot	Standard	P_0/GPa	ρ/(g/cm^3)	n_0	U_{sW}/(km/s)	P_W/GPa	T_W/kK	R_W/660 nm
018	aluminum	0.57	1.17	1.387	19.5 (0.2)	290 (9)	–	0.13 (0.03)
019	aluminum	0.63	1.18	1.39	18.2 (0.2)	241 (7)	–	0.085 (0.021)
020	aluminum	0.49	1.15	1.38	16.4 (0.2)	186 (6)	9.96 (1.20)	0.066 (0.017)
044	quartz	0.60	1.17	1.38	21.14 (0.21)	348 (10)	21.75 (2.61)	0.24 (0.06)

Two calibration methods were introduced to obtain the absolute temperature, namely, standard lamp and standard quartz. For the standard lamp, calibration was against a known standard to relate camera output C to a standard source radiance $L(\lambda)$. Calibration relied on comparison to OL455, a National Institute of Standards and Technology-traceable tungsten lamp (T ∼ 3000 K) of known spectral radiance accurate to 1%, with an emissivity of ∼ 0.003. Emissivity's uniformity is better than 98% according to the original calibration report. Although emissivity depends on wavelength, we need only the blue-channel data range (442 ± 20 nm) in both calibration and experiments. So emissivity influence and optical system response in different wavelengths can be ignored. The standard lamp was placed in the same position as the experimental target to ensure the same modulation transfer function (MTF) between calibrations and experiments. Care was

taken to ensure that the filament image was centered on the streak camera's slit. A lens (L1) was introduced in the target chamber to collect emission of the same solid angle in different experiments and calibrations. Parameters related to the streak camera's setting must be the same in calibration and experiments to ensure consistency of the SOP's transfer function. In the circumstance that calibration is performed in the same experimental configuration with laser-driven shock experiments, $L(\lambda)$ can be inferred from a simplified equation using a "dynamic calibration"[25,26] rather than "static calibration" described by Miller *et al.*[36] The equation is expressed as

$$\frac{L_{\mathrm{T}}}{L_{\mathrm{S}}} = \frac{t_{\mathrm{S}}}{t_{\mathrm{T}}} \frac{C_{\mathrm{T}}}{C_{\mathrm{S}}}, \tag{2}$$

where $L(\lambda)$ is the system's spectral radiance. Subscripts S and T represent the standard source and the laser-driven target. Due to the standard lamp's ($\sim 10^8$ W/m^3) lower spectral radiance compared with the laser-driven target ($\sim 10^{14}$ W/m^3), sweep time was set as 10 ms to ensure the intensity of response could be recorded.

For another method used in our experiments on temperature measurements, namely, standard quartz, calibration was against α -quartz with the known EOS model.[37] Because of water's transparency, we can obtain recorded self-emission intensity of both quartz and water in one shot. Water temperature can then be obtained by assuming a standard quartz model without calibration on the standard lamp. In this experiment, we used Kerley's Sesame model to achieve the temperature of quartz at the interface by adapting extracted shock velocity. The water temperature could then be expressed as

$$T_{\mathrm{W}} = \frac{hc}{\lambda k \times \ln\left[\dfrac{\varepsilon_{\mathrm{W}}}{\varepsilon_{\mathrm{Q}}} \dfrac{L_{\mathrm{Q}}}{L_{\mathrm{W}}} \left(\exp\left(\dfrac{hc}{\lambda k T_{\mathrm{Q}}}\right) - 1\right) + 1\right]}, \tag{3}$$

where subscripts Q and W represent quartz and water.

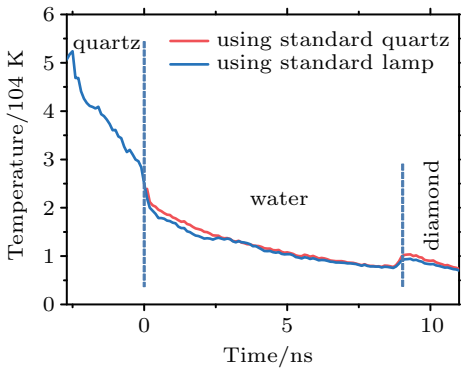

Fig. 2. (color online) Temperature as a function of time in one shot using two different methods.

Figure 2 shows these two methods' comparison in one shot. Data seem to be in good agreement, and this means both methods are reliable for measuring temperature. However, data of the relative method using standard quartz appear to have better consistency. In fact, both materials in one shot are almost in the same MTF, indicating more reliable data using the standard quartz method. In the following passage, data of shots using standard quartz are obtained from the calibration method using the EOS model of quartz, whereas data of shots using standard aluminum are obtained from adapting the standard lamp.

2.3. QMD simulations

QMD simulations predict the existence of a superionic H_2O at high pressure and low temperature.[38] Here, the Vienna *ab initio* simulation Package (VASP) is employed for QMD simulations. We use the projector augmented wave (PAW) pseudopotential and Perdew–Burke–Ernzerhof (PBE)[39] exchange–correlation functional in the QMD simulations. 54 H_2O molecules are performed in a canonical ensemble with the system's particle number, temperature and volume remaining unchanged. The energy cutoff of the plane wave is 1000 eV. The Nose–Hoover temperature regulator[40] is adapted to control the ion temperature while the electron temperature is determined by self-consistent calculation of energy occupation number's Fermi distribution. The simulation results were compared with experimental data in Figs. 4 and 5.

3. Results and discussion

Diagnostics provided measurements of shock velocity, reflectivity, and self-emission from which temperature can be extracted. Figure 3 shows diagnostic images of the one-shot experiment. Shock velocity, reflectivity, and self-emission of both materials can be achieved from VISAR and SOP systems. Time zero ($t = 0$) represents shock breakout time from the interface of quartz and water. In our experiments, velocities were measured to $\sim 1\%$ precision.[20,24,27] Reflectivity's intensity was obtained from the VISAR image's mean intensity near the target's central position. The uncertainty was $\sim 10\%$, caused by planarity, measurements of intensity, reflectivity of aluminum surface, and system error. Concretely, the reflectivity can be expressed as $R(442\ \mathrm{nm}) = R(660\ \mathrm{nm}) - d = R_{\mathrm{base}} \times C_{\mathrm{T}}/C_{\mathrm{base}} - d$, where d is the difference of reflectivity between the VISAR probe beam wavelength (660 nm) and the SOP wavelength (442 nm) and can be regarded as a constant, C_{T} is the camera output in the experiment, R_{base} and C_{base} are the reflectivity and camera output of the aluminum base, respectively. The uncertainty of C_{T} and C_{base} is $\sim 5\%$ caused by the streaked camera while the uncertainty of R_{base} is $\sim 6\%$ calculated by the target team. The root mean square of shock breakout time was ~ 6 ps,[41] indicating that planarity and stability of the shock wave was fairly good and had little effect on error. Therefore, the uncertainty of reflectivity is

$\sim$ 10% according to the error transfer formula. High reflectivity of both the shocked quartz and water that we observed suggests that they became conductive.

Figure 3(d) shows SOP's normalized intensity in one shot. The micro-channel plate and SOP slit width were 725 V and 100 μm, respectively, so that the real intensity count of self-emission obtained by SOP was not too high or too low above background with neutral density filters to ensure the streak camera's work at a linear range. We can see that the emission dropped dramatically as the shock front entered the water layer from the quartz. The diamond window's spectral response and transmissivity at the spectral range of the single channel should be taken into account. Because the boundary on SOP records was not as clear as on VISAR records because of poorer temporal resolution of $\sim$ 100 ps, the boundary on VISAR records was adapted to determine the boundary on SOP.

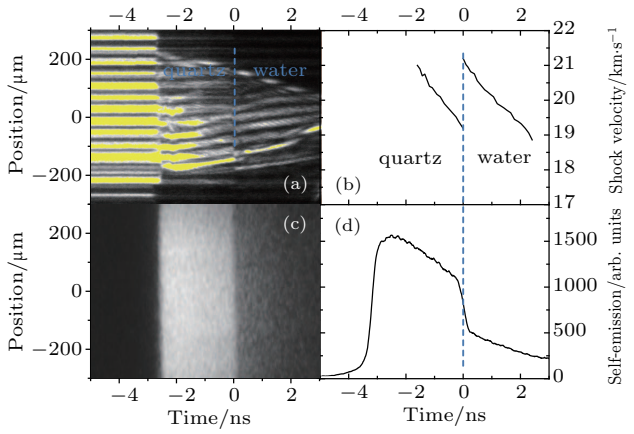

Fig. 3. (color online) Shot 044. (a) VISAR line-image record; (b) shock velocity versus time determined by VISAR; (c) SOP image record; (d) self-emission versus time determined by SOP.

Figure 4 shows shocked water's temperature data as a function of pressure, together with previous experimental works and EOS models. The interface's pressure was determined by impedance matching[28] with standard materials (aluminum or quartz), and uncertainty in pressure was $\sim$ 3% in our experiments.[24,42] This technique involves abutting the sample against the standard material of known EOS and observing the shock front as it transits the interface between the standard material and the sample. A method of inversion was used in achieving the pressure at the interface.[28] When the difference in impedance is small, the method of inversion is good in approximation, even under high pressure state. Thus, pressure up to 350 GPa was obtained as well as temperature up to 2.2×10^4 K at the interface of the standard and water sample in one shot. The experimental data agreed well with the QMD curve. Because of attenuating shock, the continuous temperature versus pressure relationship can be obtained by introducing a P–U_S relation, fitting from our data and Kimura's data[11] in which initial pressure was $\sim$ 0.5 GPa and the peak pressure reached 350 GPa in this EOS model. The P(GPa)–U_S(km/s) relation of water ($P_0 = 0.49 \sim 0.60$ GPa) can be inferred from Rankine–Hugoniot conservation equations as $P = A \times U_S + B \times U_S^2$ assuming a linear U_S–U_P relation. After fitting the data, $A = -4.9136$ and $B = 1.00301$ were obtained. This estimated relation was introduced in T–U_S relation to supplement a continuous T–P relation in our diagram. In this method, uncertainty of pressure was $\sim$ 5%, considering the fitting error of P–U_S. Therefore, both pressure calculation methods were applicable in the high pressure range we obtained. Estimated total uncertainty of temperature was 5%–12%, among which system error and measurement uncertainty were calibrated and calculated to be $\sim$ 5%. The remainder of temperature uncertainty comes from the Planck model itself.

Temperatures of precompressed water are significantly lower than those of principal Hugoniot states. Estimated continuous data and data at the shock breakout at higher final pressure (initial pressure $P_0 = 0.5$ GPa) are in very good agreement with our QMD-based EOS, but far from the Sesame. Continuous data and data at the shock breakout at lower final pressure (initial pressure $P_0 = 0.49$ GPa) are a bit higher than the model but in the range of error. These results well supported the QMD model, suggesting a superionic conductor of H_2O in icy planets' deep interior, proposing a dynamo model to explain the magnetic field structure and predicting that ice giants contain no ice, but dissociated water at high ionic conductivity.

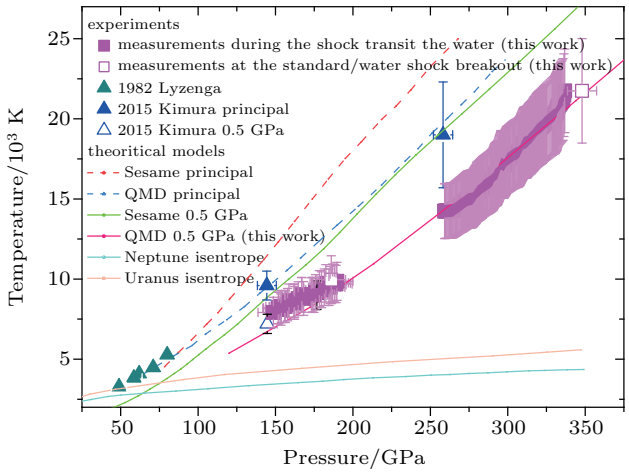

Fig. 4. (color online) Our experiment's data (pink squares) are shown with data of Lyzenga *et al.*[43] (dark cyan triangles) and Kimura *et al.*[11] (blue triangles). Also shown are theoretical models such as the Sesame model[6,11] (red dashed line for principal curve and green solid line for initial pressure at 0.5 GPa), QMD model[7–9,11] (blue dashed line for principal curve and rose solid line for $P_0 = 0.5$ GPa).

To better understand mechanisms in high-pressure water, the isochoric specific heat C_V was extracted from our off-Hugoniot data[44,45] shown in Fig. 5. Assuming that an infinitesimal section of the off-Hugoniot can be approximated as the sum of an isentropic compression step and an isochoric heating step, the variation of internal energy and temperature

can be expressed as $\Delta E_H \approx \Delta E_S + \Delta E_V$ and $\Delta T_H \approx \Delta T_S + \Delta T_V$, where subscripts H, S, and V refer to changes along the Hugoniot, isentrope, and isochore, respectively. Using definitions $P = -(\delta E/\delta V)_s$ and $\Gamma = -(V/T)(\delta T/\delta V)_s$, where P is pressure and Γ is the Gruneisen parameter, we can then write

$$C_V = \left(\frac{\Delta E_H - \Delta E_S}{\Delta T_H - \Delta T_S}\right) \approx \left(\frac{\partial E}{\partial V}\bigg|_H + P\right) \Big/ \left(\frac{\partial T}{\partial V}\bigg|_H + \Gamma \frac{T}{V}\right). \quad (4)$$

Because Γ cannot be determined independently from our data and is quite insensitive to C_V, the value estimated by Lyzenga *et al.*[43] was applied. The calculated C_V was plotted in Fig. 5. N represents the number of atoms per unit mass, and k_B is Boltzmann's constant. Our experimental data extend to a high temperature scarcely reported previously and indicate a sluggish slope gradually approaching $3Nk_B$ (Dulong–Petit limit) at high temperature. The calculated data was in good agreement with the QMD model. The degressive tendency in C_V is probably due to change in ionization and is supposedly attributed to energetics of bond breaking in the water as it transforms from a bonded molecular fluid to an ionic or superionic state at which liquid-like hydrogen ions move within a solid lattice of oxygen.

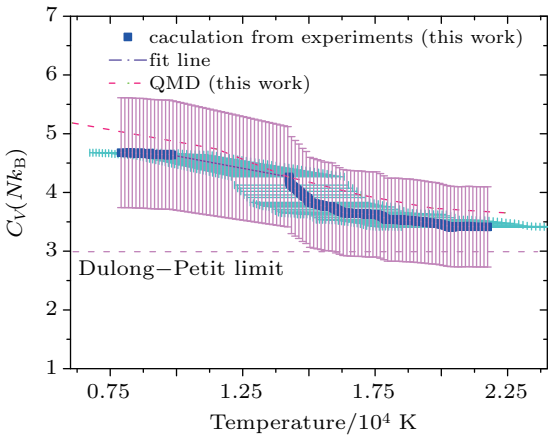

Fig. 5. (color online) The specific heat as a function of temperature.

Precompressed water's reflectivity versus shock velocity was plotted in Fig. 6(a). Data at the interface where shock transit from the standard into the water were listed in Table 1. Estimated total uncertainty in reflectivity is about 15%–25%, mainly caused by measurements of reflectivity in aluminum, reflectivity of undisturbed materials, intensity response of the camera, and system error. Our reflectivity data are lower than Celliers' principal Hugoniot data[46] at low pressure range while quite agreeing with them at high pressure. Also, our data are quite agree with Kimura's[11] at low pressure while $\sim 40\%$ higher than them at high pressure.

From Fig. 6(b), we found differences in reflectivity from different wavelengths. For the case in our experiments, emissivity ε used to determine temperature was calculated by $\varepsilon = 1 - R(660\text{ nm})$. To improve precision in temperature calculation, we used $R(442\text{ nm}) = R(660\text{ nm}) - d$ in our data processing, where d is the difference of reflectivity between the two wavelengths and 442 nm is the SOP wavelength. Corrected temperatures have already been listed in Table 1 and plotted in previously mentioned figures. The correction would cause $\sim 4\%$ uncertainty in temperature.

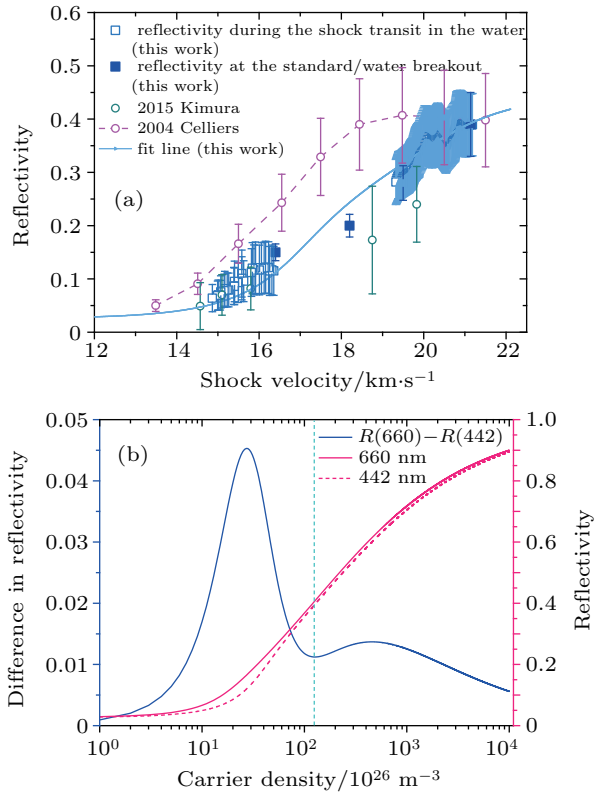

Fig. 6. (color online) (a) Reflectivity as a function of shock velocity in this work (blue squares), together with experimental data of Celliers *et al.*[46] (open pink circles) and Kimura *et al.*[11] (open green circles). Fits to our data (blue solid line) are also shown; (b) Drude reflectivity as a function of carrier density at the VISAR wavelength of 660 nm (red solid line) and SOP wavelength of 442 nm (red dashed line). Difference in reflectivity between the two wavelengths is shown by the blue line. Carrier density corresponding to the maximum reflectivity from our data is marked with a cyan dashed line.

A Drude model[46–49] was introduced to analyze shocked precompressed water's metallic properties. Optical measurements of strongly shocked dielectrics indicate that the shock front is a specular reflector whose reflectivity is suitable to Fresnel analysis, $R = |(n_s - n_0)/(n_s + n_0)|^2$, where n_s is the complex refractive index behind the shock front and n_0 is the refractive index in the undisturbed water sample, given by the empirical formula, $n_0 = 1.332 + 0.322(\rho_0 - 1)$. The complex index of refraction in a Drude model is given by $n_s^2 = 1 - (\omega_p^2/\omega^2)(1 + i/\omega\tau_e)^{-1}$, where $\omega = 2\pi c/\lambda$ is the optical frequency, τ_e is the electron relaxing time, $\omega_p = (n_e e^2/m\varepsilon_0)^{1/2}$ is the plasma frequency related to the conducting state near the Fermi surface, n_e is the effective carrier density, e is the electronic charge, $m = m_e/2$ is the reduced mass, and ε_0 is the permittivity of free space. Chemical potential is placed

midway within the gap, and the mass of holes and electrons is assumed equal. Parameters ω_p and τ_e characterize the metallic state. Electron relaxation times in fluid systems undergoing insulator–metal transitions were assumed to be near the Ioffe–Regel limit[50] given by $\tau_e = \gamma R_0/\upsilon_e$, where $R_0 = 2(3/4\pi N_i)^{1/3}$ is the interparticle spacing, $\gamma \geq 1$ and $\upsilon_e = \{2kT[F_{3/2}(-E_g/2kT)/F_{1/2}(-E_g/2kT)]\}^{1/2}$ is the electron velocity. k is the Boltzmann constant, E_g is the mobility gap energy in the electronic density of states, and $F_m(\eta) = (2/\pi^{1/2})\int x^m/[1+\exp(x-\eta)]\mathrm{d}x$. N_i is the total number of particles per unit volume. Water's Drude reflectivity can be derived as a function of n_e, as shown in Fig. 6(b). The Drude model's absorption edge is defined by $\omega_p^2(n_c) = \omega^2$, where n_c is the critical density, exceeding which high reflectivity is produced. The high reflectivity we observed suggests that the fluid becomes conductive. For the maximum reflectivity in our experiments of $R \sim 39\%$, the carrier density is $\sim 1.1 \times 10^{22}$ cm^{-3}, which is approximately 3% of the total water number density $n_{max} = 3.8 \times 10^{23}$ cm^{-3}, corresponding to a density of ~ 1.15 g/cm^3, indicating a partially ionized water at this state.

Conversely, we used carrier density in Drude formalism to model reflectivity, $n_e = 2(m_{eff}kT/2\pi\hbar^2)^{3/2}F_{1/2}(-E_g/2kT)$, where m_{eff} is the effective electron mass. The energy gap along the off-Hugoniot state is assumed a linear variation with respect to density and temperature $E_g(\mathrm{eV}) = E_0 - a(\rho/\rho_0 - 1) - b(T/T_0 - 1)$, where $E_0 \leq 6.5$.[51] After fitting the data, $a = 2.57$, $b \sim 0$, $\gamma = 1.7$, and $E_0 = 5.0024$ were obtained. Predicted reflectivity is shown in Fig. 6(a). At this time, the maximum carrier density was approximately 1.2×10^{22} cm^{-3}, which is quite consistent with the value estimated from our measured reflectivity mentioned previously.

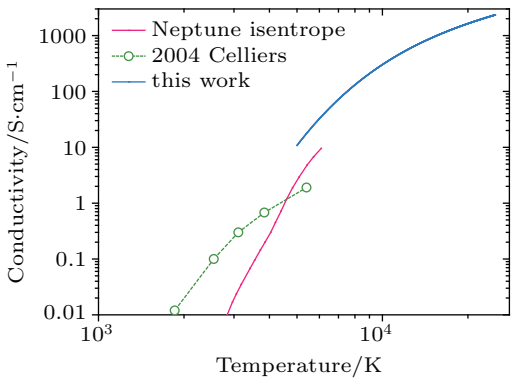

Fig. 7. (color online) Conductivity as a function of temperature calculated in this work (blue solid line). Also shown are the data of Chau *et al.*[52] rewritten by Celliers *et al.*[46] (open green circles) and the Neptune isentrope line (rose solid line).

Conductivity can be estimated by applying the Drude model $\sigma_e(\omega) = (n_e e^2 \gamma \tau_e/m)(1 - \mathrm{i}\omega\tau_e)^{-1}$, and the inferred electronic conductivity of water sample reaches $\sim$ 2000 $(\Omega\cdot\mathrm{cm})^{-1}$, as shown in Fig. 7. Also shown are the data of Chau *et al.*[52] whose temperatures were rewritten by Celliers *et al.*[46] since Celliers estimated the electronic contribution to the total DC conductivity and suggested that electronic conductivity would begin to dominate above 5000 K, and this has implications for conductivity in icy giants' interiors. In comparison with the computed σ_e along the Neptune isentrope, our estimated conductivity seems to agree with the planetary isentrope and extend the curve at higher temperature up to 2×10^4 K. The rise in water's reflectivity and its metallic-like conductivity indicate that such molecular dissociation is associated with the conducting transition. This may be an important support for planetary models using conductivity data to explain generation and development of the magnetic field in the planet's interior.

4. Conclusions

A set of experiments on measurements of shock temperature and reflectivity were carried out on water sample Up to 350 GPa and 2.1×10^4 K via VISAR and SOP using a combination of static precompression and laser-driven shock compression. In order to enhance the reliability of the SOP system, two kinds of standard were applied in calibration to measure the shock temperature. Both results were in good consistency with each other. Also, the difference in reflectivity between the VISAR probe beam wavelength and the SOP channel wavelength has been taken into account in temperature calculations to improve the precision of the data. The temperature–pressure data of precompressed water are in very good agreement with our QMD based EOS that suggesting a superionic conductor of H_2O in the deep interior of the icy planets. A degressive slope gradually approaching Dulong–Petit limit at high temperature was found in specific heat capacity and high reflectivity as well as conductivity were observed simultaneously. By synthetically analyzing the temperature–pressure relation, reflectivity, conductivity and specific heat at conditions reached in this work simulating the interior of planets, we can draw a conclusion that as the pressure rises, a change in ionization appears and is supposed to be attributed to the energetics of bond-breaking in the H_2O as the material transforms from a bonded molecular fluid to an ionic state. Such molecular dissociation in H_2O is associated with the conducting transition because the dissociated hydrogen atoms contributed to electrical properties. However, the boundary location of ionic, superionic, plasma, ice or fluid is still controversial and disputable. Further studies on experiments or theoretical works are required for detailed modeling on interior structures of planets.

Acknowledgment

We gratefully acknowledge the valuable support for the experiments by the "Shenguang-II" technical crews.

References

[1] Lara L M, Lorenz R D and Rodrigo R 1994 *Planet. & Space Sci.* **42** 5
[2] Meier R, Smith B A, Owen T C and Terrile R J 2000 *Icarus* **145** 462
[3] Surhone L M, Timpledon M T, Marseken S F and Nebula D 2010 *Astronomical & Astrophysical Transactions, the Journal of Eurasian Astronomical Society* **20** 197
[4] Hubbard W B 1997 *Science* **275** 1279
[5] Lyon S P and Johnson J D 1992 *Los Alamos Tachnical Report No. LA-UR*-92-3407
[6] Ree F H 1976 *Lawrence Livermore Laboratory Technical Report No. UCRL*-52190
[7] French M, Mattsson T R, Nettelmann N and Redmer R 2009 *Phys. Rev. B* **79** 054107
[8] French M and Redmer R 2009 *J. Phys.: Condens. Matter* **21** 375101
[9] French M, Desjarlais M P and Redmer R 2016 *Phys. Rev. E* **93** 022140
[10] Knudson M D, Desjarlais M P, Lemke R W, Mattsson T R, French M, Nettelmann N and Redmer R 2012 *Phys. Rev. Lett.* **108** 091102
[11] Kimura T, Ozaki N, Sano T, Okuchi T, Sano T, Shimizu K, Miyanishi K, Terai T, Kakeshita T and Sakawa Y 2015 *J. Chem. Phys.* **142** 109
[12] Millot M, Hamel S, Rygg J R, Celliers P M, Collins G W, Coppari F, Fratanduono D E, Jeanloz R, Swift D C and Eggert J H 2018 *Nat. Phys.* **14** 297
[13] Kimura T, Kuwayama Y and Yagi T 2014 *J. Chem. Phys.* **140** 109
[14] Stanley S and Bloxham J 2004 *Nature* **428** 151
[15] Stanley S and Bloxham J 2006 *Icarus* **184** 556
[16] Lee K K, Benedetti L R, Jeanloz R, Celliers P M, Eggert J H, Hicks D G, Moon S J, Mackinnon A, Da S L and Bradley D K 2006 *J. Chem. Phys.* **125** 1
[17] Schwager B, Chudinovskikh L, Gavriliuk A and Boehler R 2004 *J. Phys.: Condens. Matter* **16** S1177
[18] Schwager B and Boehler R 2008 *High Press. Res.* **28** 431
[19] Loubeyre P, Celliers P M, Hicks D G, Henry E, Dewaele A, Pasley J, Eggert J, Koenig M, Occelli F and Lee K M 2004 *High Press. Res.* **24** 25
[20] Shu H, Tu Y C, Wang J Y, Jia G, Ye J J, Deng W, Shu H Y, Yang Y P, Du X Y, Xie Z Y, He Z Y, Fang Z H, Hua N, Huang X G, Pei W B and Fu S Z 2018 *Acta Phys. Sin.* **67** 064101 (in Chinese)
[21] Chen W, Wang S, Mao C, Chen B and Aifen X U 1991 *Acta Opt. Sin.* **11** 829 (in Chinese)
[22] Deng X, Liang X, Chen Z, Yu W and Ma R 1986 *Appl. Opt.* **25** 377
[23] Fu S, Gu Y, Wu J and Wang S 1995 *Phys. Plasmas* **2** 3461
[24] Shu H, Fu S, Huang X, Wu J, Xie Z, Zhang F, Ye J, Jia G and Zhou H 2014 *Phys. Plasmas* **21** 2162
[25] Zhiyu H, Huazhen Z, Xiuguang H, Guo J, Hua S, Zhiheng F, Junjian Y and Zhiyong X 2016 *High Power Laser Part. Beams* **28** 28042002
[26] He Z Y, Jia G, Zhang F, Luo K, Huang X G, Shu H, Fang Z H, Ye J J, Xie Z Y, Xia M and Fu S Z 2018 *Eur. Phys. J. D* **72** 3
[27] Shu H, Fu S Z, Huang X G, Fang Z H, Wang T, Ye J J, Xie Z Y, Zhou H Z and Long T 2012 *Eur. Phys. J. D* **66** 1
[28] Celliers P M, Collins G W, Hicks D G and Eggert J H 2005 *J. Appl. Phys.* **98** 113529
[29] Mao H K, Bell P M, Shaner J W and Steinberg D J 1978 *J. Appl. Phys.* **49** 3276
[30] Shimizu H, Nabetani T, Nishiba T and Sasaki S 1996 *Phys. Rev. B* **53** 6107
[31] Hua Shu J W, Yuchun Tu, Xiuguang Huang, Zhiyu He, Guo Jia, Junjian Ye, Zhiyong Xie, Fan Zhang, Sizu Fu (unpublished)
[32] Spaulding D K 2010 *Laser-Driven Shock Compression Studies of Planetary Compositions* (Berkeley: Graduate Division of the University of California)
[33] Glukhodedov V D and Kirshanov S I 1999 *J. Exp. Theor. Phys.* **89** 292
[34] Kormer S B 1968 *Soviet Phys. Usp.* **11** 229
[35] Zhou X, Nellis W J, Li J, Li J, Zhao W, Liu X, Cao X, Liu Q, Xue T and Wu Q 2015 *J. Appl. Phys.* **118** 043524
[36] Miller J E, Boehly T R, Melchior A, Meyerhofer D D, Celliers P M, Eggert J H, Hicks D G, Sorce C M, Oertel J A and Emmel P M 2007 *Rev. Sci. Instrum.* **78** 034903
[37] Kerley G I 1999 *Equations of state for composite materials* (Albuquerque: Kerley) p. 1
[38] Cavazzoni C, Chiarotti G L, Scandolo S, Tosatti E, Bernasconi M and Parrinello M 1999 *Science* **283** 44
[39] Perdew J P, Burke K, Ernzerhof M, Perdew J P, Burke K and Ernzerhof M 1996 *Phys. Rev. Lett.* **77** 3865
[40] Hoover G 2007 *Mol. Simulation* **33** 13
[41] Shu H, Fu S Z, Huang X G, Ma M X, Wu J, Ye J J, He J H and Gu Y 2007 *Eur. Phys. J. D* **44** 367
[42] Zhang H, Duan X X, Zhang C, Liu H, Zhang H G, Xue Q X, Ye Q, Wang Z B and Jiang G 2016 *Chin. Phys. Lett.* **33** 086202
[43] Lyzenga G A, Ahrens T J, Nellis W J and Mitchell A C 1982 *J. Chem. Phys.* **76** 6282
[44] Hicks D G, Boehly T R, Eggert J H, Miller J E, Celliers P M and Collins G W 2006 *Phys. Rev. Lett.* **97** 025502
[45] Eggert J H, Hicks D G, Celliers P M, Bradley D K, Mcwilliams R S, Jeanloz R, Miller J E, Boehly T R and Collins G W 2010 *Nat. Phys.* **6** 40
[46] Celliers P M, Collins G W, Hicks D G, Koenig M, Henry E, Benuzzi-mounaix A, Batani D, Bradley D K, Silva L B D and Wallace R J 2004 *Phys. Plasmas* **11** L41
[47] Hicks D G, Celliers P M, Collins G W, Eggert J H and Moon S J 2003 *Phys. Rev. Lett.* **91**
[48] Huser G, Recoules V, Ozaki N, Sano T, Sakawa Y, Salin G, Albertazzi B, Miyanishi K and Kodama R 2015 *Phys. Rev. E* **92** 063108
[49] Celliers P M, Loubeyre P, Eggert J H, Brygoo S, Mcwilliams R S, Hicks D G, Boehly T R, Jeanloz R and Collins W G 2010 *Phys. Rev. Lett.* **104** 184503
[50] Ioffe A F and Regel A R 1960 *Prog. Semicond.* **4** 237
[51] Williams F, Varma S P and Hillenius S 1976 *J. Chem. Phys.* **64** 1549
[52] Chau R, Mitchell A C, Minich R W and Nellis W J 2001 *J. Chem. Phys.* **114** 1361